



Article

Influences of Different Factors on Gravity Wave Activity in the Lower Stratosphere of the Indian Region

Jialiing Hou ¹ , Jia Luo ^{1,2,*} and Xiaohua Xu ^{1,3}

¹ School of Geodesy and Geomatics, Wuhan University, 129 Luoyu Road, Wuhan 430079, China; jialiinghou@whu.edu.cn (J.H.); xhxu@sgg.whu.edu.cn (X.X.)

² China Key Laboratory of Geospace Environment and Geodesy, Ministry of Education, 129 Luoyu Road, Wuhan 430079, China

³ Collaborative Innovation Center for Geospatial Technology, 129 Luoyu Road, Wuhan 430079, China

* Correspondence: jialuo@whu.edu.cn

Abstract: The gravity wave (GW) potential energy (E_p) in the lower stratosphere (LS) of the altitude range between 20 and 30 km over the Indian region (60°E – 100°E , 0° – 30°N) is retrieved using the dry temperature profiles from the Constellation Observing System for Meteorology Ionosphere and Climate-2 (COSMIC-2) radio occultation (RO) mission from December 2019 to November 2021. Through correlation analysis and dominance analysis (DA) methods, the impacts of multiple influencing factors on the local LS GW activity are quantified and compared. The results demonstrate that in the central and northern part of Indian region, the three factors, including the convective activity (using outgoing long-wave radiation as the proxy) mainly caused by the Indian summer monsoon, the mean zonal wind speed between 15 and 17 km, the height range where the maximum tropical easterly jet (TEJ) wind speed appears, and the mean zonal wind speed between 20 and 30 km, have the greatest impacts on the LS GW activity. In the southern part of the Indian Peninsula and over the Indian Ocean, the mean zonal wind shear between 20 and 30 km plays a dominant role in the LS GW activity, which is due to the fact that the GW energy can be attenuated by large background wind shears. It can be concluded that the LS GW activity in the Indian region is mainly influenced by the Indian summer monsoon, the TEJ, and the wind activity in the LS, while over different local areas, differences exist in which factors are the dominant ones.

Keywords: gravity wave (GW); lower stratosphere (LS); Indian region; radio occultation (RO); COSMIC-2; dominance analysis (DA) method



Citation: Hou, J.; Luo, J.; Xu, X.

Influences of Different Factors on Gravity Wave Activity in the Lower Stratosphere of the Indian Region.

Remote Sens. **2024**, *16*, 761. <https://doi.org/10.3390/rs16050761>

Academic Editors: Michael E. Gorbunov, Vladimir Gubenko, Pawel Gilewski and Xiaolei Zou

Received: 12 January 2024

Revised: 12 February 2024

Accepted: 19 February 2024

Published: 22 February 2024



Copyright: © 2024 by the authors. Licensee MDPI, Basel, Switzerland. This article is an open access article distributed under the terms and conditions of the Creative Commons Attribution (CC BY) license (<https://creativecommons.org/licenses/by/4.0/>).

1. Introduction

Gravity waves (GWs), the fluctuations generated by buoyancy and gravity under stable stratification in the atmosphere, transfer energy, momentum, atmospheric constituents and water vapor in fluid environments, depositing vertical mixing of heat [1–3]. The propagation of GWs in the atmosphere is affected by various dissipation processes, and the energy and momentum carried by GWs are stored in the background atmosphere, which further affects the local and global atmospheric thermodynamic and dynamic processes [4,5]. As a key driving mechanism in the middle and lower atmosphere through drag and diffusion processes, GW activity plays an important role in the global circulation and atmospheric system [2,6,7] and must be considered in global circulation models (GCMs) to reproduce the real atmospheric structure [5,8,9]. At present, it is still difficult to explicitly solve GWs and their associated eddy diffusion in GCMs due to the computational power and required cost [10–13]. Therefore, obtaining the GW parameters through observations is of great importance, which will improve the accuracy and reliability of the predictions of GCMs. Satellite observations, which are valuable complements to traditional ground-based

and field observations, can provide global information about the spatial and temporal distributions of GWs and make it possible to provide some constraints on the parameterization of GW activity in GCMs [13].

Global navigation satellite system (GNSS) radio occultation (RO), which is a satellite-based observation technology developed rapidly in the last two decades, can provide atmospheric and ionospheric products with global coverage, all-weather capability, and long-term stability. The vertical resolution of RO temperature profiles ranges from 100 m in the lower troposphere to 1.4 km in the upper stratosphere. The RO temperature profiles generally have errors of less than 0.4 K in the upper troposphere and lower stratosphere (UTLS) [14–16], which are ideal data sources for the study of GWs in this altitude region [2,17–19].

The Formosa Satellite-7/Constellation Observing System for Meteorology, Ionosphere, and Climate-2 (FORMOSAT-7/COSMIC-2, hereafter COSMIC-2) mission, a Taiwan–United States GNSS RO mission, was launched on 25 June 2019 [20]. The six satellites of COSMIC-2 were deployed in 24° inclination parking orbits at an altitude of about 550 km [21,22], each of which carries an advanced Tri-GNSS RO System instrument (TGRS) developed by the National Aeronautics and Space Administration’s Jet Propulsion Laboratory [23]. COSMIC-2 is the successor to the highly successful COSMIC mission, whose products have improved global weather forecasts and supported hundreds of scientific studies of weather, climate, and space weather [2,16,24–26]. After the COSMIC-2 mission is fully operational, it will observe about 5000 RO events per day at middle and low latitudes of 40°S–40°N. Compared to COSMIC, which can only observe the global positioning system (GPS) RO events, COSMIC-2 can observe both the GPS and the global navigation satellite system (GLONASS) RO events, and the performance of the RO receivers has been improved substantially [20,21,27]. The large volume of high-quality temperature profiles retrieved from the COSMIC-2 RO atmospheric observations are valuable data sources for extracting reliable GW parameters in the lower stratosphere (LS) of the subtropical and tropical regions, based on which the sources of GWs over these regions can be further investigated.

GWs can be generated from various sources, such as flow over topography, wind shear, jet stream, and atmospheric convection, and can propagate from the unstable airflow in the lower atmosphere to the middle and upper atmosphere under the influence of the background wind [7,28,29]. In previous studies, some scholars have studied the sources of GWs and the influencing factors in some local regions. Based on the data from a mesosphere–stratosphere–troposphere (MST) radar station in Gadanki, tropical India, Ratnam et al. [30] analyzed the energy mechanisms generating the inertial GWs over this station and suggested that the main factors which affect the GWs over Gadanki are convection, jet flow, and wind shear. Zhang et al. [31] studied the GW activity in the stratosphere over the globe based on the eight-year SABER/TIMED temperature observations, and they pointed out that deep convection is the main source for the observed tropical GWs and that wind also influences the tropical GW activity. Randel et al. [27] used COSMIC-2 RO data to study the spectra of different equatorial waves in the tropical tropopause and lower stratosphere, including the Kelvin waves, the mixed Rossby gravitational waves, the inertial gravitational waves, the diurnal tide, and the small-scale GWs caused by frequent continental convection and topography, and they pointed out that the GWs in the altitude range of 18–20 km over several tropical regions within the latitudes of 16°S–0° are closely related to convection. In previous works that investigated the factors influencing regional GWs, the spatiotemporal distributions of GW parameters and those of each potential factor were usually compared qualitatively. Although some studies presented the correlation coefficients between the GW parameters and the potential influencing factors [24,30,32], none of them quantified the relative importance of different factors on the GW activity.

To investigate the importance of different factors on the GW activity of a local area, it is better that the main factors that have significant impacts on the GW activity of this area are identified. The Indian region (60°E–100°E, 0°–30°N) is a specific area characterized by its distinct monsoon phenomenon [33]. From June to September each year, the Indian summer monsoon, which contains large amounts of water vapor, blows from the Indian Ocean

to the Indian Peninsula, and the interaction between the monsoon and the mountainous terrain generates convections in the Indian region. Some studies have found that there is a strong correlation between GWs and convections, which are strongly correlated with the Indian monsoon [30,33,34]. The variation of GWs in the LS is significantly affected by the accompanying background wind field, which has been recorded in the Indian region [34–36]. Moreover, the tropical easterly jet (TEJ) prevails over this region during the monsoon period, with its maximum zonal wind speed appearing at a height of around 16 km [37,38]. It has been noticed that the TEJ leads to the formation of strong zonal wind shears in the troposphere, which generate GWs, and the upward propagation of the waves further enhances the GWs in the LS [30,39]. Other studies found that when strong tropical cyclones originate from the Bay of Bengal and the Indian Ocean land on the Indian Peninsula, the convections near the cyclone path are strengthened, thus enhancing the activity of GWs [26,34]. Based on these previous studies, the present work aims to further investigate the relative importance of the main factors that affect the GWs in the LS of the Indian region and to quantify the relative contributions of these factors. Moreover, we also try to analyze the possible physical mechanisms of some influencing factors on the LS GWs in this region.

The remainder of this paper is organized as follows. Section 2 introduces the data and methods, including the COSMIC-2 RO data and other data used in this study; the methods for deriving the GW potential energy (E_p) from the RO temperature profiles and for constructing the gridded datasets of the GW E_p in lower stratosphere of 20–30 km (simplified as LS hereafter) and the influencing factors; and the dominance analysis (DA) method for quantifying the contributions of influencing factors to the LS GWs. Section 3 presents the main results. In this section, the spatial and temporal variations of the mean GW E_p between 20 and 30 km over the Indian region are shown, based on which the distributions of the Pearson correlation coefficients (CCs) and the DA coefficients, which are obtained, respectively, by carrying out correlation analysis and the dominance analysis on the time series of the LS GW E_p and the influencing factors, are further presented. The impacts of the selected factors on LS GWs in the Indian region and the geographic difference in the impacts of two factors, the zonal wind and wind shear, on the LS GWs of the Indian region, are discussed in Section 4. Section 5 presents the conclusions.

2. Data and Methods

By using the COSMIC-2 RO temperature data from December 2019 to November 2021, we obtain the GW E_p profiles in the Indian region, based on which the LS GWs activity in this region is analyzed, and the influences of the main factors, including the wind, the wind shear, and the convection, on the LS GWs are systematically investigated. Note that considering the impact of TEJ on the LS GWs in the studied region, besides the mean wind and wind shear between 20 and 30 km, the mean wind and wind shear in the height range of the core of TEJ that the maximum zonal wind speed appears, i.e., 15–17 km, are also considered as the main influencing factors. We use the CCs to represent the correlation between each factor and the LS GW E_p , and for the first time, by using the DA method, the relative importance of each factor on the LS GWs is quantified, and the individual contributions of different factors are presented.

2.1. Data

The COSMIC-2 temperature profiles (the so-called dry temperature retrievals, atmPrf, near real-time version 0001.0001) in the latitudes of 5°S–35°N from December 2019 to November 2021, which are obtained from the COSMIC Data Analysis and Archive Center (CDACC), are used to extract the GW E_p profiles over the Indian region (60°E–100°E, 0°–30°N). Note that considering the requirements for the retrieval of the GW E_p profiles and for the construction of the three-dimensional (3D) LS GW E_p grid field, the geographic area covered by the selected RO data is wider than the studied region.

In addition to the RO data, the monthly winds of the same period, distributed at 37 pressure levels between 1000 hPa and 1 hPa with the horizontal resolution of $0.25^\circ \times 0.25^\circ$ (longitude \times latitude), provided by the European Centre for Medium-Range Weather Forecasts (ECMWF) Reanalysis v5 (ERA5) dataset (CF-1.6 Conventions), are used to calculate the monthly gridded zonal/meridional winds and wind shears over the Indian region. The monthly gridded outgoing long-wave radiation (OLR) data, with a horizontal resolution of $2.5^\circ \times 2.5^\circ$ (CF-1.2 Conventions), is obtained from the National Oceanic and Atmospheric Administration (NOAA) Climate Diagnostics Center (CDC) and is used as the proxy for convection.

2.2. GW E_p Extracted from the COSMIC-2 Temperature Profiles

When investigating the characteristics of GWs based on satellite observations, GW energy is usually used as a proxy parameter for GW activity [2,13,18], which includes the kinetic energy (E_k) and the potential energy (E_p). According to the linear wave theory, the ratio of the kinetic energy to the potential energy (E_k/E_p) is approximate to a constant in the atmosphere. Therefore, the GW activity can be directly characterized by GW E_p [18,40]. In the present study, for each RO temperature profile, the corresponding GW E_p profile is derived using the horizontal detrending method, and the GWs with vertical wavelengths larger than twice the vertical resolution of RO observations (around 1 km) are extracted by this method.

The steps for retrieving the GW E_p profiles using the dry temperature profiles are briefly introduced as follows. First, each raw dry temperature profile is interpolated with an interval of 0.1 km, and the horizontal position corresponding to the profile is designated as the mean longitude and latitude within the height range of 20–30 km. Then, for each day, over the whole latitude range of 5°S – 35°N , all the interpolated temperature profiles are binned into $5^\circ \times 5^\circ$ longitude \times latitude grids and the daily mean temperature profile for each grid is derived, which corresponds to the horizontal position of the center point in the grid. Based on the daily mean temperature profiles of all the grids, the daily 3D temperature grid field in the altitude range of 20–30 km is constructed. At each height level between 20 and 30 km, the zonal wavenumbers 0–6 of each 5° latitude band in the daily 3D temperature grid field are extracted by applying the S-transform, based on which the daily 3D background temperature grid field, with the resolution of $5^\circ \times 5^\circ \times 0.1$ km, is constructed. Through interpolating in the background temperature grid field, the background temperature profile \bar{T} of each raw dry temperature profile T is obtained, and the corresponding temperature perturbation profile T' caused by GWs is derived as $T - \bar{T}$. For each temperature perturbation profile T' , the corresponding GW E_p profile is derived using Equation (1).

$$E_p = \frac{1}{2} \frac{g^2}{N^2} \left(\frac{T'}{\bar{T}} \right)^2 \quad (1)$$

where g is the gravitational acceleration, and N is the Brunt–Väisälä frequency calculated based on \bar{T} . For more details on the method for extracting GW E_p from raw temperature profiles, please refer to Wang and Alexander [41,42] and our previous works [43,44].

Note that quality checks are carried out on both the original atmPrf files and the derived GW E_p profiles. The atmPrf data files marked as “bad” by CDAAC in the global attribute and the GW E_p profiles with non-physical values exceeding the range of 0–50 J/kg within the altitudes between 20 and 30 km are excluded. In the latitudes of 5°S – 35°N during December 2019 and November 2021, there are 1,907,379 raw COSMIC-2 dry temperature profiles, from which 1,756,160 qualified GW E_p profiles are obtained. In order to obtain spatial information on GW activities at a more detailed scale, the qualified E_p profiles are gridded into the boxes with a longitude \times latitude resolution of $2.5^\circ \times 2.5^\circ$. For each $2.5^\circ \times 2.5^\circ$ grid, 33 qualified GW E_p profiles are obtained per month on average, which is sufficient to construct the GW E_p monthly average grid data.

2.3. Construction of the 3D Grids for Monthly LS GW Ep and Influencing Factors

Using the qualified GW Ep profiles derived from the COSMIC-2 temperature data, the spatiotemporal 3D grid dataset of the monthly averaged GW Ep for the height range of 20–30 km over the Indian region is obtained. First, the studied region (0° – 30° N, 60° E– 100° E) is gridded into $2.5^{\circ} \times 2.5^{\circ}$ (longitude \times latitude) bins. Then, the monthly averaged GW Ep profile corresponding to each grid point is derived by averaging all the qualified GW Ep profiles within the $5^{\circ} \times 5^{\circ}$ region centered on it. For example, the averaged GW Ep profile for the grid point of (10° N, 80° E) is calculated by averaging the qualified GW Ep profiles in the four bins of (7.5° – 10° N, 77.5° – 80° E), (7.5° – 10° N, 80° – 82.5° E), (10° – 12.5° N, 77.5° – 80° E), and (10° – 12.5° N, 80° – 82.5° E). There will be an overlap between the $5^{\circ} \times 5^{\circ}$ area corresponding to a certain grid point and its neighboring grid points. This is based on the method proposed in [13]. For each month, the monthly averaged LS GW Ep value for a specific grid point is obtained by averaging the GW Ep values at all the height levels between 20 and 30 km. Finally, the spatiotemporal 3D grid data of the monthly averaged LS GW Ep, which has a resolution of $2.5^{\circ} \times 2.5^{\circ} \times 1$ month, is obtained for the studied area during December 2019 and November 2021.

To study the contribution of each considered factor to the LS GW activities in the Indian region, the 3D grid data with a resolution of $2.5^{\circ} \times 2.5^{\circ} \times 1$ month is also prepared for the proxy of each influencing factor. Nine factors are considered, including the OLR, which represents the convection; the mean zonal (meridional) wind and wind shear in the height range of 20–30 km, which represent the background wind field; and the mean zonal (meridional) wind and wind shear in the height range of 15–17 km, which represent the TEJ.

The OLR data from the NOAA CDC, which is used as the proxy for convection, is provided directly with a resolution of $2.5^{\circ} \times 2.5^{\circ} \times 1$ month. The monthly zonal (meridional) wind speed field from the ERA 5, which has a horizontal resolution of $2.5^{\circ} \times 2.5^{\circ}$, is interpolated with the height interval of 0.1 km at first. At each grid point and for each height level, the monthly zonal (meridional) wind shear, which refers to the magnitude of the change in wind speed in the vertical direction [30], is calculated as the derivative of the monthly zonal (meridional) wind speed to height by using Equations (2) and (3) [45].

$$us_i = \frac{du}{dz} = \frac{u_{i+1} - u_i}{z_{i+1} - z_i} \quad (2)$$

$$vs_i = \frac{dv}{dz} = \frac{v_{i+1} - v_i}{z_{i+1} - z_i} \quad (3)$$

where i is the height level number in the wind speed profile, dz is the vertical resolution of the interpolated wind speed profile, which is equal to 0.1 km here to be consistent with the vertical resolution in calculating GW Ep, u and v are the zonal and meridional wind profiles, respectively, and us_i and vs_i are the zonal and meridional wind shears at the i th height level. Note that the eastward (northward) wind phase is defined as the positive direction of the zonal (meridional) wind speed and wind shear. At each $2.5^{\circ} \times 2.5^{\circ}$ grid point, the monthly averaged zonal (meridional) wind speeds and zonal (meridional) wind shears for each of the two height ranges, 15–17 km and 20–30 km, are obtained by averaging the monthly wind speeds and wind shears at all the height levels of the corresponding height range.

Finally, we construct the $2.5^{\circ} \times 2.5^{\circ} \times 1$ -month 3D grid data fields for the LS GW Ep over the Indian region and for the nine influencing factors. We denote the set of the factors as $\mathbf{X} = [X_1, X_2, \dots, X_p]$ with $p = 9$, and the LS GW Ep is denoted as Y . Based on the 3D grid data of \mathbf{X} and Y , the correlation between each influencing factor and GW Ep can be calculated, and the relative importance of each factor on the LS GWs over the Indian region will be further evaluated.

2.4. Correlation Analysis and Dominance Analysis

At each $2.5^\circ \times 2.5^\circ$ grid point, the correlation analysis is carried out between the time series of each factor in \mathbf{X} , which varies from December 2019 to November 2021 with a step of 1 month (24 months in total), and the time series of LS GW Ep, based on which the spatial distribution of the Pearson correlation coefficients (CCs) between each factor and LS GW Ep over the Indian region is obtained.

In addition to the correlation analysis, the DA method is further applied to evaluate the influences of the nine different factors on the LS GWs over the Indian region by using the time series of each factor in \mathbf{X} and the time series of Y . The DA method, which is developed based on the multiple linear regression (MLR) model, can be used to evaluate the relative importance of a single factor in the MLR model by examining the change in R^2 (coefficient of determination) resulting from adding a predictor to all possible subset regression models [46–48]. As a supplement to the regression analysis, when there is multicollinearity between independent variables, the dominance analysis can de-emphasize redundant predictors, thus reducing the impact of collinearity between independent variables and better representing the statistical contribution of independent variables [49,50]. Similar to correlation analysis, for each grid point in the Indian region, the time series of each factor in \mathbf{X} and those of LS GW Ep (denoted as Y) are used to build an MLR model:

$$Y = a_0 + a_1X_1 + a_2X_2 + \dots + a_pX_p + e \quad (4)$$

where $p = 9$ is the influencing factors number, a_0, a_1, \dots, a_p are the regression coefficients, and e is the residual. There are 2^p possible subset models containing various possible combinations of these factors. Let \mathbf{X}_{-i} represent a subset of \mathbf{X} that does not contain the factor X_i , and the coefficient of determination (R^2) of the model subset \mathbf{X}_{-i} is represented by $R_{Y|\mathbf{X}_{-i}}^2$. For all possible subsets \mathbf{X}_{-i} , the difference between the coefficient of determination (R^2) of the model subsets with and without the factor X_i , denoted as $Diff_R_{X_i}^2(\mathbf{X}_{-i}) = R_{Y|X_i\mathbf{X}_{-i}}^2 - R_{Y|\mathbf{X}_{-i}}^2$, are calculated, and the contribution of the factor X_i , which denotes as C_{X_i} , is the average of $Diff_R_{X_i}^2(\mathbf{X}_{-i})$ for all possible subsets \mathbf{X}_{-i} . The value of C_{X_i} is non-negative, and the larger the value of C_{X_i} , the higher the explanatory power of X_i in predicting Y . Therefore, C_{X_i} can be regarded as the relative importance coefficient (RIC) of the factor X_i . The sum of the RICs of all factors should equal the R^2 of the MLR model [47,48,51]. By applying the dominance analysis over all the $2.5^\circ \times 2.5^\circ$ grid points, the spatial distributions of the RICs of all the nine influencing factors that affect the LS GWs over the Indian region are obtained.

3. Results

3.1. GW Climatology in the Indian Region

Figure 1 presents the seasonal variation in the latitude–longitude distributions of the mean LS GW Ep over the Indian region during December 2019 and November 2021. The four seasons are defined as MAM (March–May), JJA (June–August), SON (September–November), and DJF (December–February). For the whole Indian region, the mean LS GW Ep is distinctly larger in JJA than in other seasons, and the peak mean LS GW Ep appears over the central part of the Indian Peninsula in JJA. On the one hand, as demonstrated by previous studies [30,39,52,53], the peak mean LS GW Ep over the Indian region is closely related to the TEJ, which is prevalent in this region in JJA. The strong wind shears generated by TEJ are important sources of local GWs. On the other hand, in JJA, the Indian summer monsoon blowing from the ocean to the land brings large amounts of water vapor, enhancing the local convections and creating favorable conditions for the generation and propagation of GWs. In the following section, further analysis is carried out to investigate the relative importance of some main factors related to TEJ and monsoon activity, such as convective activity, average meridional wind speeds of 15–17 km, mean zonal wind speeds of 20–30 km and wind shear, on LS GW activity in the Indian region. In contrast, during

the other seasons, the mean LS GW Ep over the Indian Ocean near the equator is generally larger than that over the Indian Peninsula.

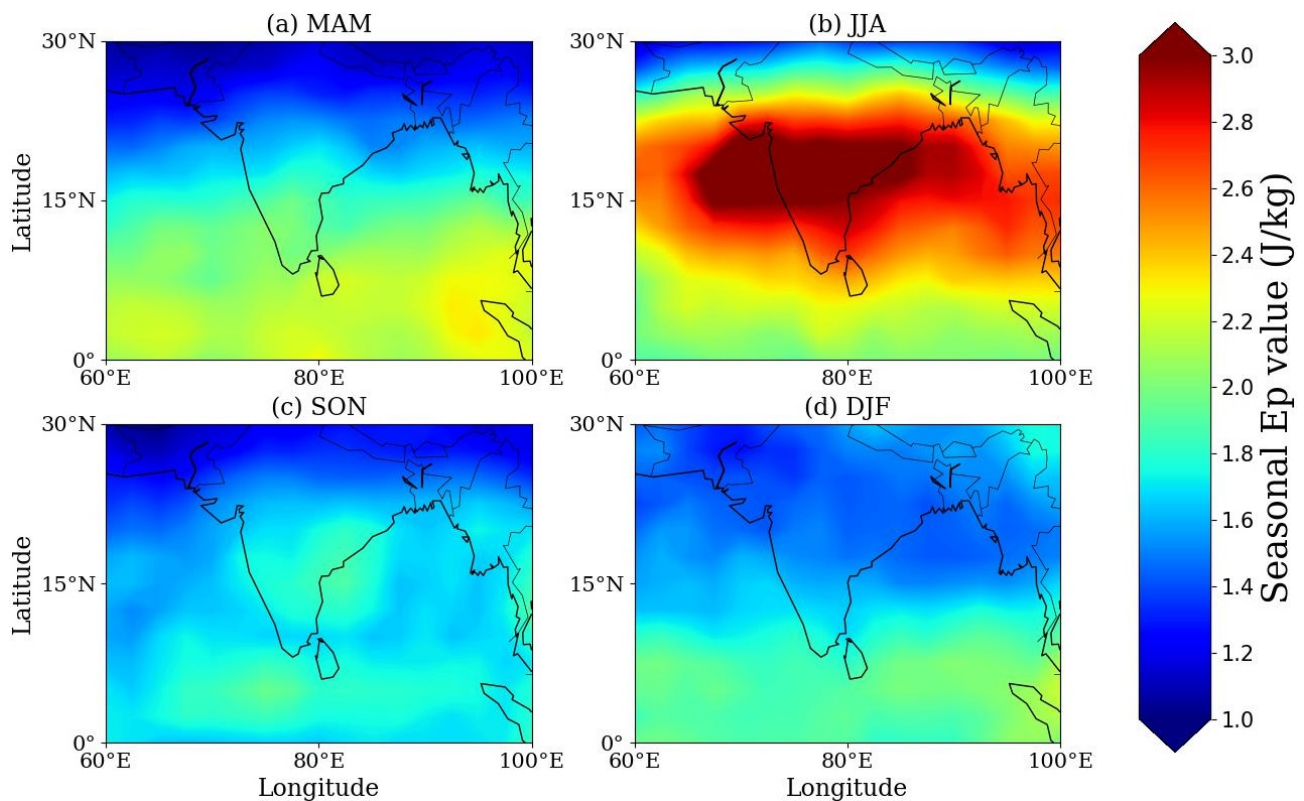


Figure 1. Latitude–longitude distributions of the mean LS GW Ep over the Indian region in different seasons: (a) MAM, (b) JJA, (c) SON, and (d) DJF during December 2019 and November 2021.

3.2. Distributions of the CCs and RICs of Different Influencing Factors

Figure 2 shows the latitude–longitude distributions of the CCs between the mean LS GW Ep and each of the nine factors. In most areas of the Indian Peninsula, the mean LS GW Ep is strongly negatively correlated with the mean eastward wind speeds in both of two height ranges, 15–17 km (Figure 2a) and 20–30 km (Figure 2e), with the CCs generally smaller than -0.4 . It is also negatively correlated with the OLR (Figure 2i), which is the proxy for convective activity. Over the Bay of Bengal and its surrounding land area, the mean LS GW Ep is also negatively correlated with the mean northward wind speeds between 15 and 17 km (Figure 2b) and 20 and 30 km (Figure 2f), while the influence of the mean northward wind speed between 20 and 30 km on the mean LS GW Ep is not as strong as the mean northward wind speed between 15 and 17 km according to the magnitudes of the CCs. In the northern part of the Indian Peninsula, the mean LS GW Ep has positive correlations with the mean eastward wind shear between 15 and 17 km (Figure 2c), generally with the CCs between 0.3 and 0.6. In the middle and southern parts of the Indian Peninsula and over the Indian Ocean, strong positive correlations exist between the mean LS GW Ep and the mean eastward wind shear in the 20–30 km height range (Figure 2g), with the CCs generally higher than 0.5. Over the Bay of Bengal and its surrounding land area, the mean LS GW Ep is positively correlated with the mean northward wind shear between 15 and 17 km (Figure 2d) and the mean eastward wind shear between 20 and 30 km (Figure 2g), generally with the CCs of 0.3–0.6. In comparison, over the Indian Peninsula and the Bay of Bengal, the correlations between the mean LS GW Ep and the mean northward wind shears in the 20–30 km height range (Figure 2h) are comparatively smaller, mostly with the CCs of 0–0.4.

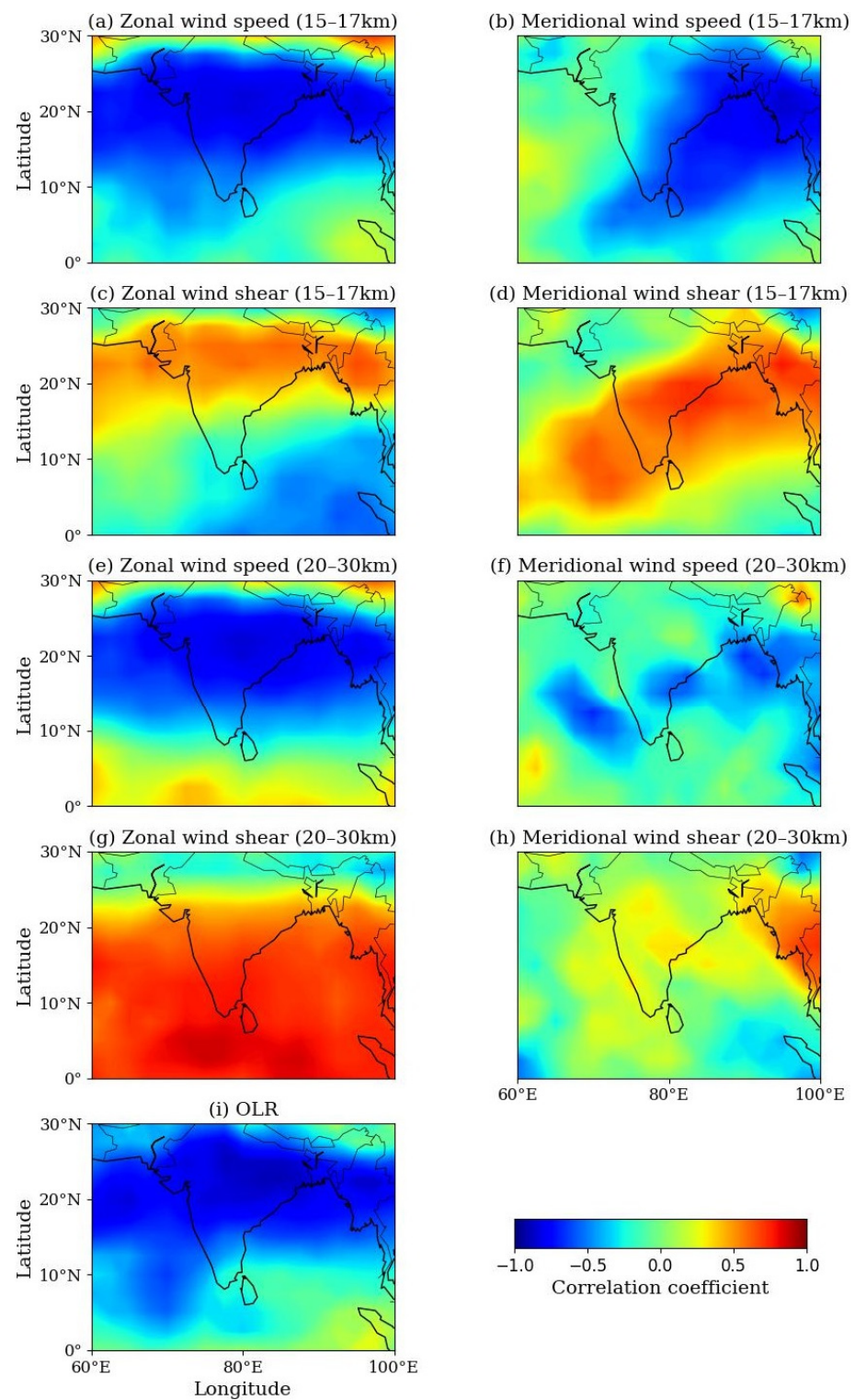


Figure 2. Latitude–longitude distributions of the CCs between the time series of the mean LS GW Ep and those of the nine influencing factors over the Indian region during December 2019 and November 2021. The nine influencing factors are (a) 15–17 km zonal wind speed; (b) 15–17 km meridional wind speed; (c) 15–17 km zonal wind shear; (d) 15–17 km meridional wind shear; (e) 20–30 km zonal wind speed; (f) 20–30 km meridional wind speed; (g) 20–30 km zonal wind shear; (h) 20–30 km meridional wind shear; and (i) OLR as the proxy of convection activity, respectively. The eastward/northward wind phases are defined as positive of zonal/meridional winds.

Figure 2 demonstrates that over the Indian Peninsula, the mean LS GW Ep has strong correlations with different factors, and the correlations might be positive or negative. The correlation analysis above indicates that these factors should play important roles in the generation and propagation of GWs over the Indian region, which is consistent with previous studies [30,39,53].

However, it is not objective enough to evaluate the influence of each factor on the LS GW activity only according to the magnitudes of the CCs. For example, in the central region of the Indian Peninsula between 15°N and 25°N, the mean wind speeds in the two altitude ranges, 15–17 km and 20–30 km, and OLR all have strong negative correlations with the mean LS GW Ep, with their CCs generally smaller than -0.4 . On the other hand, in the same region, the mean zonal wind shears between 15 and 17 km, 20 and 30 km, and the mean meridional wind shears between 15 and 17 km all have strong positive correlations with the mean LS GW Ep, with the CCs generally larger than 0.4 . It is difficult to evaluate the relative importance of the above factors on the LS GW activity in this region based on the CCs only. In addition, due to the possible collinearities among these influencing factors, it is difficult to present the individual contribution of each factor to the LS GW activity objectively through the Pearson correlation coefficient solely. The DA method helps reduce the influence of the possible collinearity among independent variables on the analyzing results, as mentioned in Section 2.4. In Fang et al. [54], the DA method is adopted instead of the Pearson correlation coefficient to quantify the relative importance of different driving factors that affect the density variations of different elements in the Martian upper atmosphere. In the present study, to further quantify the contribution of each factor to the LS GWs over the Indian region, using the DA method, the RICs of each factor over each $2.5^\circ \times 2.5^\circ$ grid point are calculated, based on which the latitude–longitude distributions of the RICs of the nine factors are obtained, as presented in Figure 3.

The RICs of the nine factors generally vary between 0 and around 0.55, and the maximum RIC is obtained by the factor of the mean zonal wind shear in the 20–30 km altitude range (Figure 3g) over the Indian Ocean. The distributions of the RICs of different factors demonstrate that over the Indian region, local differences exist in the main factors influencing the LS GW activity.

Generally, in the central and northern parts of the Indian Peninsula, the relative importance of the convection (Figure 3i) is the greatest, followed by the mean zonal wind speeds between 15 and 17 km (Figure 3a) and 20 and 30 km (Figure 3e). In the southern part of the Indian Peninsula and over the Indian Ocean, the impact of the mean zonal wind shear between 20 and 30 km (Figure 3g) on the LS GWs is dominant, and the meridional wind speed and the mean zonal wind shear between 15 and 17 km (Figure 3b,c) also have some contributions to the LS GW activities over the Indian Ocean. Over the Bay of Bengal and its surrounding land area, the mean meridional wind speed between 15 and 17 km (Figure 3b) has an important impact on the LS GWs.

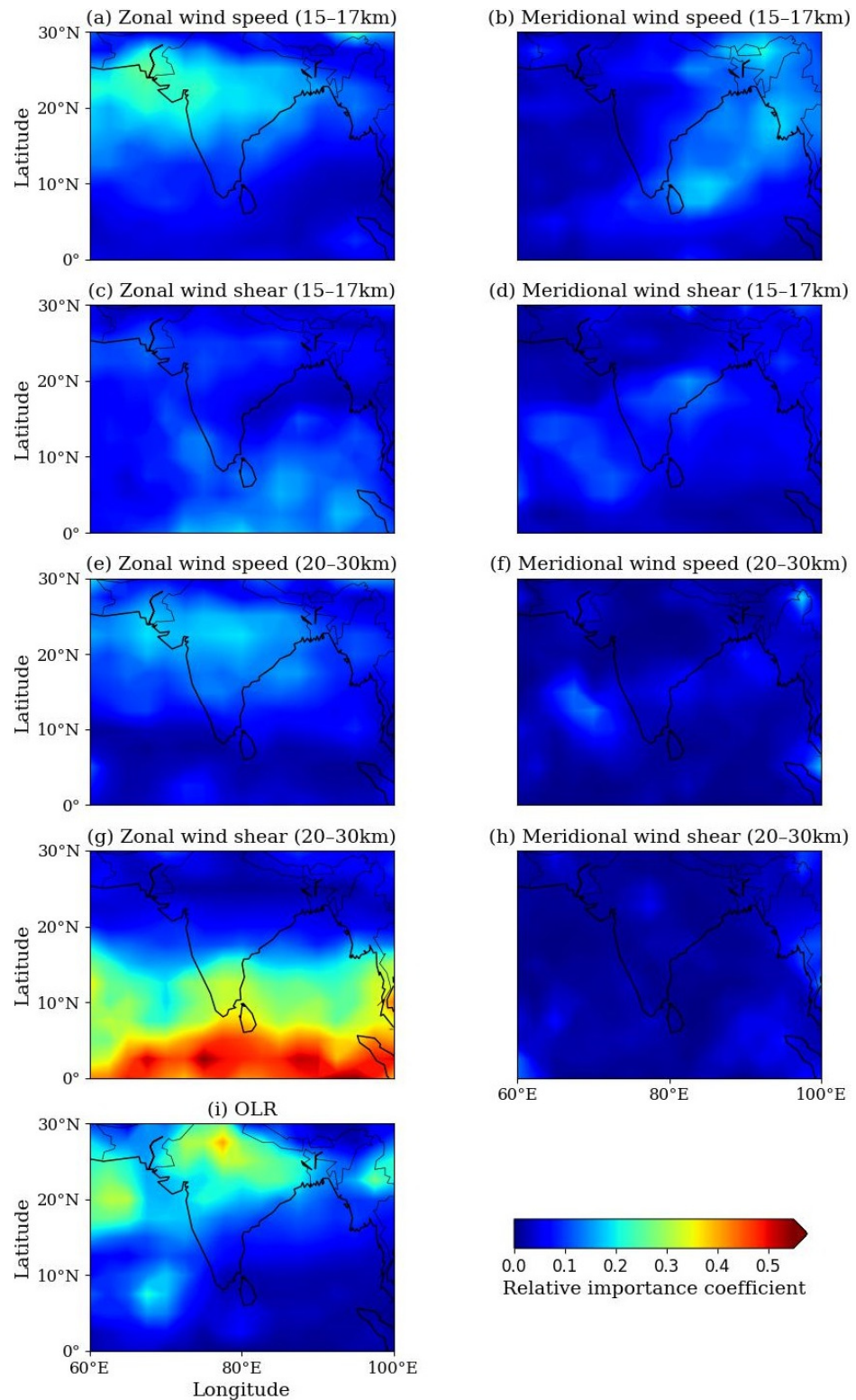


Figure 3. Latitude–longitude distributions of the RICs of the nine influencing factors of the LS GW activities over the Indian region during December 2019 and November 2021. The nine influencing factors are (a) 15–17 km zonal wind speed; (b) 15–17 km meridional wind speed; (c) 15–17 km zonal wind shear; (d) 15–17 km meridional wind shear; (e) 20–30 km zonal wind speed; (f) 20–30 km meridional wind speed; (g) 20–30 km zonal wind shear; (h) 20–30 km meridional wind shear; and (i) OLR as the proxy of convection activity, respectively. The eastward/northward wind phases are defined as positive of zonal/meridional winds.

Specifically, in the central and northern parts of the Indian Peninsula, the factor with the largest RICs is convection, using OLR as the proxy parameter (Figure 3i), and the RICs of convection generally reach above 0.2, even exceeding 0.4 in the southern foothills of the Himalayas. This should be mainly attributed to the fact that the interaction of the Indian summer monsoon circulation and the terrain of the Himalayas results in frequent convective systems over the northern part of the Indian Peninsula, especially in the arch-shaped belt region along the terrain features of the southern Himalayan front [55,56], which becomes an important source of the GWs here. The factor with the second largest RIC values is the mean zonal wind speed between 15 and 17 km (Figure 3a), which shows that the TEJ in the summer season is indeed an important source of the LS GWs over these areas. The RICs of the mean zonal wind speed between 20 and 30 km (Figure 3e) are mainly within the range of 0.15–0.25, which are generally slightly smaller than those of the mean zonal wind speed between 15 and 17 km. As for the southern tip of the Indian Peninsula and the Indian Ocean, the RICs of the mean zonal wind shear between 20 and 30 km (Figure 3g) are significantly larger than those of the other factors, generally reaching higher than 0.3, which demonstrates that the mean zonal wind shear between 20 and 30 km is the most important factor influencing the LS GWs in this region. Moreover, the mean meridional wind speed between 15 and 17 km (Figure 3b) and the mean zonal wind shear between 15 and 17 km (Figure 3c) also show some influences on the LS GWs in this region, with the RICs varying between 0.10 and 0.25. Over the Indian Ocean near the southwest of the Indian Peninsula, the influence of the convections (Figure 3i) on LS GWs is also non-negligible. In comparison, over the Bay of Bengal and its surrounding land area, the contribution of the mean meridional wind speed between 15 and 17 km (Figure 3b) to the LS GWs is comparatively significant, with the RICs varying between 0.10 and 0.25.

It can be found that the RICs of the three factors, including the mean meridional wind speed between 20 and 30 km (Figure 3f), the mean meridional wind shear between 20 and 30 km (Figure 3h), and the mean meridional wind shear between 15 and 17 km (Figure 3d), are generally smaller than 0.2, indicating that these factors are not the dominant ones influencing the LS GWs over the whole studied area. Overall, based on the distributions of the RICs of different factors, it is clear that over the whole Indian region, the influences of the zonal wind speeds and the zonal wind shears in the two height ranges (Figure 3a,c,e,g) on the LS GWs are generally much greater than those of the meridional wind speeds and wind shears in the two height ranges (Figure 3b,d,f,h). Moreover, it can also be inferred from the RIC distributions that the LS GWs in the central and northern parts of the Indian Peninsula are more affected by the zonal wind speeds (Figure 3a,e) than by the zonal wind shears (Figure 3c,g), while the situation is opposite in the southern part of the Indian Peninsula and over the Indian Ocean, where the RICs of the zonal wind shears in the two height ranges are generally higher. In order to gain a deeper understanding of why the influences of the zonal wind-related factors on the LS GWs over the Indian region show spatial differences, two sample grid points, which are, respectively, located in the northern and the southern parts of the Indian Peninsula, are selected, and the impacts of zonal wind speeds and wind shears on the LS GWs over these two grid points are analyzed and are compared in Section 4.2.

4. Discussion

4.1. Quantification of the Impacts of Selected Factors on LS GW Activities in the Indian Region

As mentioned in Section 2.4, the sum of the RICs of all factors equals to the total R^2 of the MLR model. The determination coefficient R^2 may vary between 0 and 1, and the closer R^2 is to 1, the better the independent variable set X in the MLR model can explain the dependent variable Y . Figure 4 presents the spatial distribution of the sums of the RICs of all the nine considered factors, and the closer the sum of the RICs to 1, the greater the combined influence of these factors is. As can be seen, except for the latitude band between 25°N and 30°N in the northern part of the Indian region, where the sums of the RICs vary between 0.4 and 0.6, the sums of the RICs are generally higher than 0.7 in the

Indian Peninsula, the Bay of Bengal and its surrounding land area, and the Indian Ocean. This demonstrates that the factors considered in the present study, including the TEJ with its jet core in the height range of 15–17 km, the air flows between 20 and 30 km, and the convections that are closely related to the Indian summer monsoon are, indeed, the main factors affecting the LS GWs in most part of the Indian region. This is also consistent with previous studies [30,39,53]. The latitude band of around 5° in the northern part of the region, where the summed RICs are generally lower, is mainly the Himalayas and Qinghai–Tibet Plateau with large terrain heights. Both the distributions of the CCs shown in Figure 2 and those of the RICs shown in Figure 3 demonstrate that the LS GWs in this area are mostly affected by the convective activity, while they are less affected by the TEJ and the air flows between 20 and 30 km.

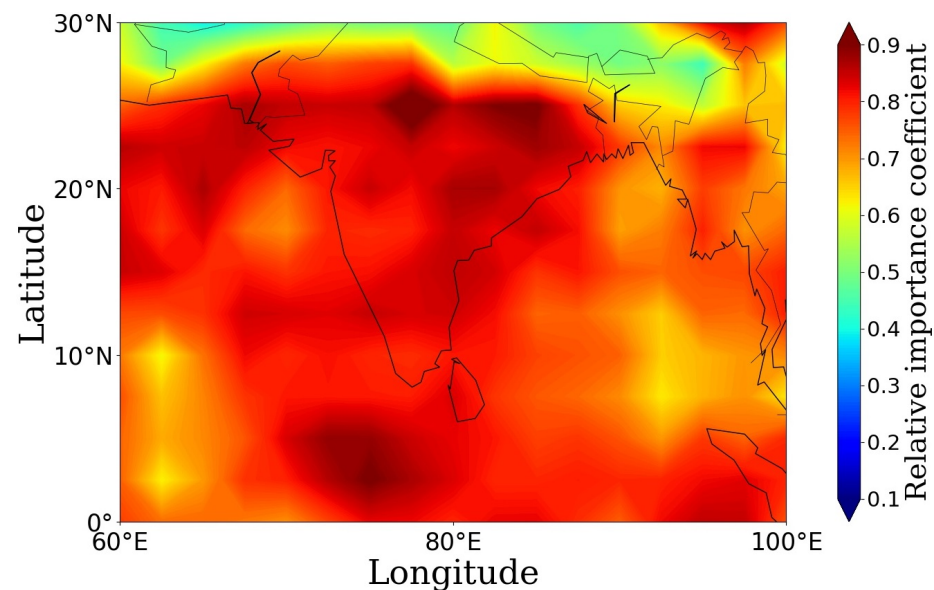


Figure 4. Latitude–longitude distribution of the sums of the RICs of all the nine influencing factors over the Indian region during December 2019 and November 2021.

4.2. Analysis of the Impacts of Zonal Wind Speeds and Wind Shears on the LS GWs in Different Local Regions

The results presented in Section 3 demonstrate that over the Indian region, the wind flows and the wind shears in the two height ranges, 15–17 km (TEJ) and 20–30 km, and the convection are generally the main factors influencing the LS GWs, while over different local areas, differences exist in which factors are the dominant ones. More specifically, among the wind-related factors, the influences of the zonal wind-related factors are greater than those of the meridional wind-related factors in most local areas, while regional differences exist on which zonal wind-related factors are the dominant ones. This aspect and the possible mechanisms will be further discussed in this section, and two grid points are selected as the representatives for different geographic locations. As presented in Figure 5a, grid point A (77.5°E, 10°N) is located at the southern end of the Indian Peninsula, and grid point B (80°E, 22.5°N) is located in the middle of the Indian Peninsula. According to the distributions of the RICs of each factor presented in Figure 3, the zonal wind shear between 20 and 30 km plays a dominant role in influencing the LS GWs at grid point A, while at grid point B, the zonal wind speeds between 15 and 17 km and 20 and 30 km both have relatively important impacts on the LS GWs.

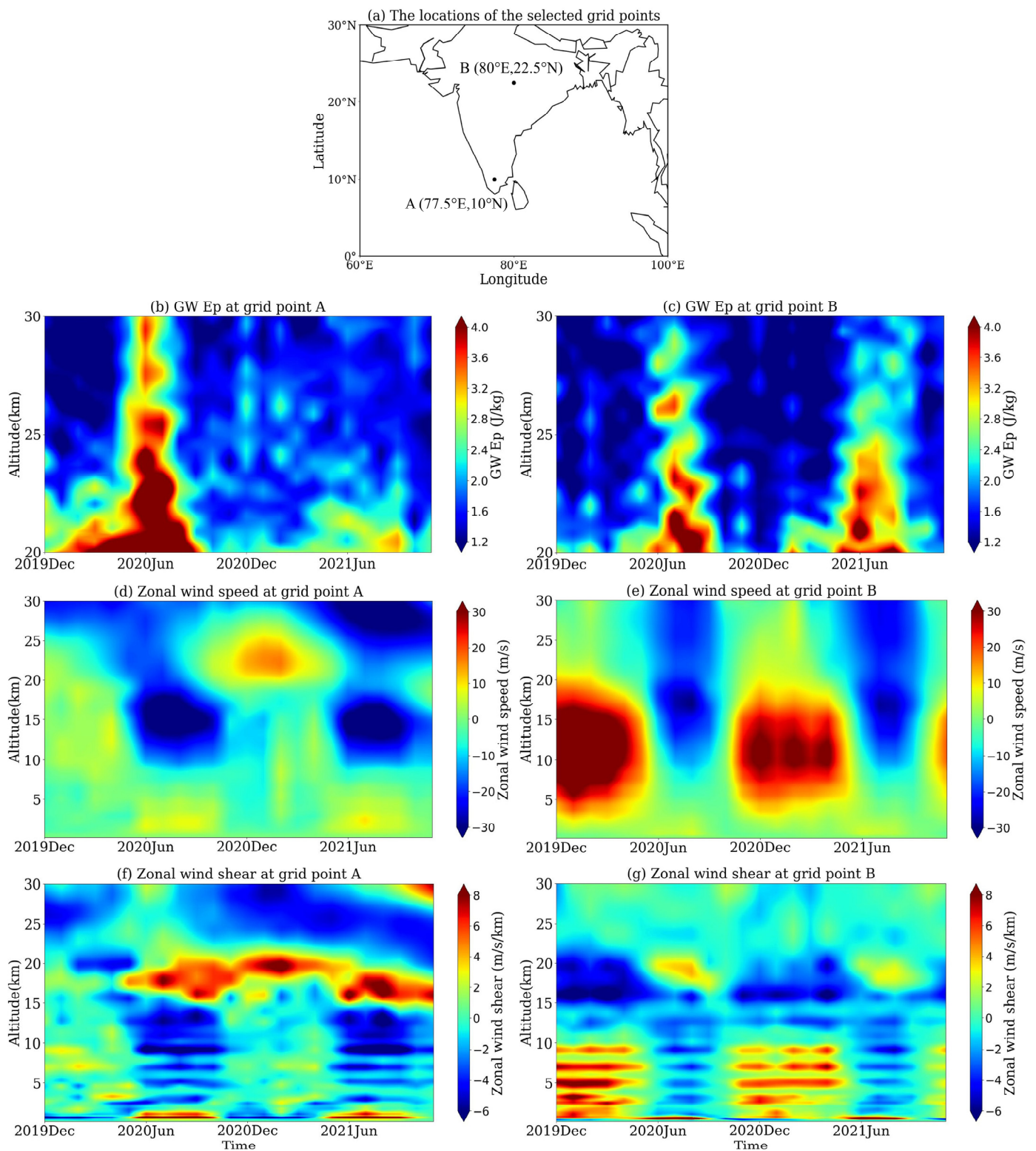


Figure 5. Geographic locations of two representative grid points in the Indian Region (a), and the altitude–time distributions of GW Ep (b,c), zonal wind speeds (d,e), and zonal wind shears (f,g) over the two grid points during December 2019 to November 2021. The eastward wind phases are defined as positive of zonal wind speed and zonal wind shear.

Figure 5b–g show the altitude–time distributions of the GW Ep, the zonal wind speeds, and the zonal wind shears over these two grid points. As we can see in Figure 5d,e, during JJA of 2020 and 2021, the westward wind phases appear at altitudes higher than 10 km

over both of the two grid points and the maximum wind speeds appear at around 16 km, reaching higher than 20 m/s, which is due to the TEJ being prevalent over the Indian region in JJA [30,39]. At the same time, the easterly wind shears are generated within a height range of about 16–20 km above the two grid points (see Figure 5f,g), which becomes one of the important sources of the GWs in the LS of the Indian region, and, influenced by the strong westward winds, the GWs generated propagate to higher than 20 km. The altitude-time distributions of GW Ep over the two grid points, which are shown in Figure 5b,c, both present peak GW Ep during JJA. This is attributed to the contributions of both the TEJ and the convection activity. As we can see in Figure 3a,i, at grid point B, the magnitudes of the RIC of the mean zonal wind speed between 15 and 17 km (0.19) and that of the OLR (0.22) are close, which indicates that the contributions of the two factors to the high GW Ep over this grid point are similar. However, at grid point A, the RIC of the mean zonal wind speed between 15 and 17 km and that of OLR are 0.09 and 0.03, respectively, which indicates that between the two factors, the contribution of TEJ on the GW Ep is greater than that of convective activity and that at this grid point, the impacts of both of the two GW source factors on the LS GWs are very limited ($\text{RIC} < 0.1$).

Figure 5b indicates that at grid point A, during JJA of both years, due to the contributions of the two GW source factors, the mean zonal wind speed between 15 and 17 km and the convection activity, high GW energy is generated at the heights lower than 20 km. Figure 3a,i reveal that for the LS GW activity, i.e., GWs between 20 and 30 km, the RICs of the two source factors are both very low, and this should be mainly due to the significant influence of the background LS zonal wind shear on the upward propagation of the GW energy.

During JJA of 2020 at grid point A, the high GW energy propagates up to the whole height range of 20–30 km, while during JJA of 2021, the high GW energy propagates upward only to the height of about 22–23 km and then dissipates, which should be mainly attributed to the large westward wind shears in the 22–28 km height range above this grid point, considering that the GW energy can be attenuated by large background wind shears [34,57–59]. Figure 5d shows that during JJA of 2021, the zonal wind speeds of 14–18 km and those above 25 km over grid point A are very close, both of which are westward winds with speeds higher than 30 m/s, but the westward wind speeds at 18–23 km are generally less than 15 m/s. The large differences between the zonal wind speeds in the 18–23 km height range and those of the upper and lower altitude regions result in large zonal wind shears, especially between 22 and 28 km during JJA of 2021, as shown in Figure 5f, which are beneficial for the filtering of GWs. In comparison, during JJA of 2020, at this grid point, the zonal wind shears are generally very small at altitudes higher than 20 km, and so the GWs can propagate up to 30 km and higher, as presented in Figure 5b.

Figure 6 further presents the time series of the mean LS GW Ep and the mean zonal wind shear between 20 and 30 km at grid point A. They both reach peak values in JJA of 2020, and the CC between them is 0.78, indicating a strong positive correlation between the mean LS GW Ep and the mean zonal wind shear in the 20–30 km height range at this grid point. Figure 6 also shows that at grid point A, the peak value of the mean zonal wind shear between 20 and 30 km obtained in JJA of 2020 is around 0 m/s, which provides stable atmospheric conditions favorable for the upward propagation of the high GW energy generated mainly by TEJ at around 16 km in the stratosphere. During the other time periods, the mean zonal wind shears between 20 and 30 km over grid point A are generally westward, and the filtering effect of the background wind should bring the dissipation of the high GW energy, which explains the distinct reduction of GW Ep at the altitudes higher than around 23 km at this grid point in JJA of 2021. Figure 5b,d,f and Figure 6 together should explain the high RICs of the mean zonal wind shear between 20 and 30 km around grid point A, as presented in Figure 3.

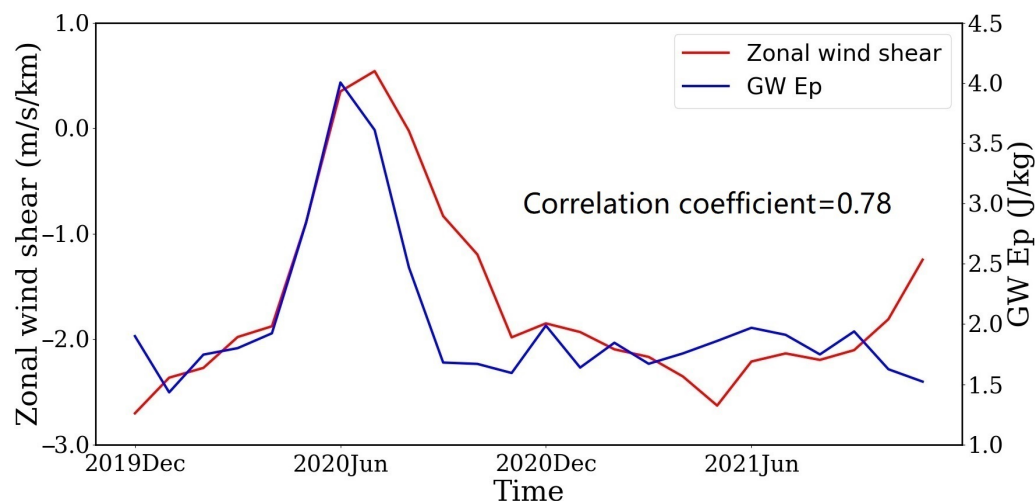


Figure 6. The time series of the mean zonal wind shear at 20–30 km and mean LS GW Ep at grid point A during December 2019 and November 2021.

In comparison, at grid point B, GW energy propagates upward to the height of around 30 km during JJA of both 2020 and 2021, as shown in Figure 5c. As revealed by the comparison of Figure 5c,e, at grid point B, during JJA of both years, the peak GW Ep at 20–30 km is generally accompanied by strong westward winds in the whole altitude range of 10–30 km. Note that, besides the core of TEJ between 15 and 17 km, strong westward winds also prevail at higher altitudes between 17 and 30 km, which facilitate the upward propagation of GWs. Miyahara et al. [60] pointed out that strong background winds should contribute to the upward propagation of GWs, and the propagation of the GW energy generated in the troposphere to the stratosphere under strong background winds has been observed in previous studies [2,18,61]. Moreover, as presented in Figure 5g, the zonal wind shears formed in the whole altitude range of 20–30 km are generally very small, which is also beneficial for the high GW energy to propagate to higher than 30 km. At grid point B, during JJA of both years, besides the small zonal wind shear between 20 and 30 km, the strong background wind field in the UTLS provides one of the important GW sources (TEJ) and the favorable conditions for the upward propagation of GWs, which should partly explain the comparatively high RICs of the mean zonal winds between 15 and 17 km and 20 and 30 km at this grid point, as presented in Figure 3.

Note that the propagation and the filtering effect of the background wind field on GW should be identified more clearly by the correlation between the background wind direction and the propagation direction of GW. For example, it is very clear that over grid point A, westward winds are very strong beyond 20 km in JJA 2021, which could have attenuated the upward propagating GWs. As proposed by [62], westward waves propagate freely through eastward wind, and if there is a reversal phenomenon in the background wind field, the westward propagating GWs are easily filtered by the westward wind, and vice versa. This probably indicates that GWs are mostly propagating westward at grid point A over 20 km during JJA 2021. Figure 7 further shows the time–longitude distribution of the mean GW Ep value between 20 and 21 km at 10°N in the Indian region, and at grid point A, this height range is just below the strong westward wind shear. A fact that may support the westward propagation of GWs at 10°N during JJA 2021 is that GW Ep reaches peak values higher than 2.8 J/kg in the latitude range of 80°E–100°E while decreasing significantly within the latitude range of 60°E–80°E during this period. It can be reasonably inferred that the GWs propagate from east to west and gradually dissipate due to the strong shear caused by strong westward winds above 20 km at 10°N during JJA in 2021. Furthermore, it may indicate that during JJA 2021, over grid point A, which is at 10°N, the westward propagating GWs only propagate upwards to around 22–23 km and are filtered out by strong westward winds in the higher altitude.

However, since E_p is scalar, inferring the propagation direction of GW through the peak distribution of E_p is only conjecture, and the true propagation direction of gravity waves can only be obtained through spectral analysis of GWs. As proposed by [63,64], the latitudinal component of the horizontal wavenumber of LS GW in the Indian region can be derived by using the triples of COSMIC-2 dry temperature profiles under strict spatiotemporal constraints. From December 2019 to November 2021, there were only 17 eligible triples of profiles in the Indian region (60°E – 100°E , 0° – 30°N), making it difficult to derive reasonable and statistically significant GW parameters that can depict the direction of GW propagation directions over this region. Using appropriate data for spectral analysis of GW to further investigate the propagation direction of GW and its correlation with background wind fields in the Indian region will be the goal of our next work.

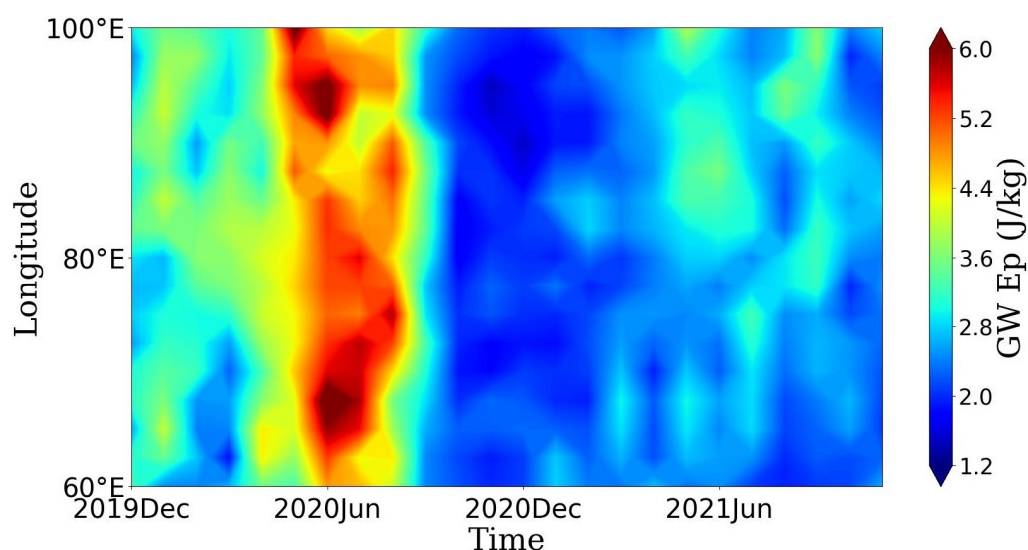


Figure 7. The time–longitude distribution of the mean GW E_p value between 20 and 21 km at 10°N in the Indian Region.

5. Summary and Conclusions

By using the COSMIC-2 RO dry temperature profiles from December 2019 to November 2021, the GW E_p profiles in the LS of the Indian region (60°E – 100°E , 0° – 30°N) are derived, based on which the seasonal variation of the LS GWs in the height range of 20–30 km (abbreviated as the LS GWs) is presented, and the correlations between the mean LS GW E_p and nine influencing factors are analyzed. The influence of each factor is further quantified using the DA method, which outperforms correlation analysis in evaluating the individual contribution of each factor when collinearity exists in the influencing factors.

The LS GWs in the Indian region show distinct annual variations, and the maxima of the mean LS GW E_p appears in JJA. Generally, the TEJ, which prevails over the Indian region during JJA, and the Indian summer monsoon, which enhances the local convection activity, both bring favorable conditions for the generation and propagation of GWs. The correlation analysis reveals that in the Indian region, most of the selected factors have a strong correlation with LS GW, indicating that the selected factors have an undeniable impact on LS GW activity, at least in certain parts of the Indian region. If there are strong correlations between LS GW activity and multiple factors in a specific area, it is difficult to quantify the relative influence of these factors based on CCs only. The distributions of the RICs obtained with the DA method demonstrate that the factors that are of great relative importance on the LS GWs vary in different geographic areas of the Indian region. Specifically, in the central and the northern parts of the Indian region, especially in the southern foothills of the Himalayas, the contribution of convection activity is the greatest, which should be due to the interaction of the Indian summer monsoon circulation and the terrain of the Himalayas in summer. The mean zonal wind speed between 15 and 17 km

is the factor with the second greatest relative importance, indicating that the TEJ, which prevails over the Indian region during JJA, is an important source for the LS GWs. The mean zonal wind speed between 20 and 30 km also has a non-negligible influence. In the southern part of the Indian Peninsula and over the Indian Ocean, the mean zonal wind shear between 20 and 30 km is the dominant factor influencing the LS GWs. The dominance analysis also reveals that the influences of the zonal wind speeds and the zonal wind shears on the LS GWs are different over different local areas of the Indian region.

The sums of the RICs of all the nine considered factors are generally higher than 0.7, which may demonstrate that in most parts of the Indian region, the TEJ with the core in the height range of 15–17 km, the air flows between 20 and 30 km, and the convections that are closely related to the Indian summer monsoon are actually the main factors affecting the LS GWs. Further analysis of the impacts of zonal wind speeds and wind shears on the LS GWs in different local regions showed that, in the southern part of the Indian Peninsula and over the Indian Ocean, strong westward wind shear generated over 20 km may have a filtering effect on gravity waves propagated from below, making it difficult for GWs to propagate to above 23 km during the 2021 JJA. Therefore, wind shear becomes the dominant factor in the GW activity in this region. In the central and northern parts of the Indian region, due to the absence of strong wind shear, gravity wave energy propagated upwards to 30 km during the JJA of 2020 and 2021. The RIC values of the mean zonal wind speed between 15 and 17 km, which represents the wave source of TEJ, and the mean zonal wind speed between 20–30 km, which represents the propagation conditions, become higher.

It should be mentioned that due to the lack of sufficient triples of COSMIC-2 profiles that meet the spatiotemporal constraints, it is hard to derive further the propagation direction of gravity waves in the present work, which will be the goal of our next research work. Moreover, the terrain is not considered an independent influencing factor, which is because the correlation analysis and the dominance analysis are based on the time series of the multiple factors and GW E_p , and the temporal variations of terrain heights are not significant. Furthermore, it is reasonable to assume that the impact of terrain on GWs is partially implied in the convective activity generated by the interaction between terrain in the Indian region and the Indian summer monsoon. In future work, we will further explore in detail the impact of terrain on GWs in the Indian region. In addition, we will also apply the DA method to the GW source studies of the other monsoon regions in the future, such as the East Asian monsoon region and the monsoon region in northern Australia, by using the datasets from multi-RO missions.

Author Contributions: Conceptualization, X.X.; Investigation, J.L. and J.H.; Methodology, J.H.; Project administration, J.L. and X.X.; Supervision, J.L. and X.X.; Writing—original draft, J.L. and J.H.; Writing—review and editing, X.X. All authors have read and agreed to the published version of the manuscript.

Funding: This work is supported by the National Natural Science Foundation of China (Grant Nos. 42174017, 42074027, 41774033 and 41774032).

Data Availability Statement: The data used in the manuscript are all public data. The atm-Prf data of the COSMIC-2 RO missions were downloaded from the CDAAC Data Center: <https://cdaac-www.cosmic.ucar.edu/cdaac/products.html> (last accessed on 11 January 2024). The ERA5 reanalysis dataset was downloaded from the ECMWF: <https://www.ecmwf.int/en/forecasts/datasets/reanalysis-datasets/era5> (last accessed on 11 January 2024). The monthly gridded outgoing long-wave radiation (OLR) data were obtained from the National Oceanic and Atmospheric Administration (NOAA) Climate Diagnostics Center (CDC): <https://psl.noaa.gov/data/gridded/data.olrcdr.interp.html> (last accessed on 11 January 2024).

Acknowledgments: The authors would like to express their gratitude to the University Corporation for Atmospheric Research (UCAR) for providing the COSMIC-2 data. We are also very grateful to the NOAA Climate Diagnostics Center and the ECMWF for providing the data of OLR and the ERA5 reanalysis dataset, respectively.

Conflicts of Interest: The authors declare no conflicts of interest.

References

1. John, S.R.; Kumar, K.K. TIMED/SABER observations of global gravity wave climatology and their interannual variability from stratosphere to mesosphere lower thermosphere. *Clim. Dyn.* **2012**, *39*, 1489–1505. [[CrossRef](#)]
2. Hindley, N.P.; Wright, C.J.; Smith, N.D.; Mitchell, N.J. The southern stratospheric gravity wave hot spot: Individual waves and their momentum fluxes measured by COSMIC GPS-RO. *Atmos. Chem. Phys.* **2015**, *15*, 7797–7818. [[CrossRef](#)]
3. Zhang, Y.; Zhang, S.; Huang, C.; Huang, K.; Gong, Y.; Gan, Q. The interaction between the tropopause inversion layer and the inertial gravity wave activities revealed by radiosonde observations at a midlatitude station. *J. Geophys. Res. Atmos.* **2015**, *120*, 8099–8111. [[CrossRef](#)]
4. Manzini, E.; McFarlane, N.A. The effect of varying the source spectrum of a gravity wave parameterization in a middle atmosphere general circulation model. *J. Geophys. Res. Atmos.* **1998**, *103*, 31523–31539. [[CrossRef](#)]
5. Alexander, M.J.; Geller, M.; McLandress, C.; Polavarapu, S.; Preusse, P.; Sassi, F.; Sato, K.; Eckermann, S.; Ern, M.; Hertzog, A.; et al. Recent developments in gravity-wave effects in climate models and the global distribution of gravity-wave momentum flux from observations and models. *Q. J. R. Meteorol. Soc.* **2010**, *136*, 1103–1124. [[CrossRef](#)]
6. Holton, J.R. The influence of gravity wave breaking on the general circulation of the middle atmosphere. *J. Atmos. Sci.* **1983**, *40*, 2497–2507. [[CrossRef](#)]
7. Fritts, D.C.; Alexander, M.J. Gravity wave dynamics and effects in the middle atmosphere. *Rev. Geophys.* **2003**, *41*, 1003. [[CrossRef](#)]
8. Kim, Y.; Eckermann, S.D.; Chun, H. An overview of the past, present and future of gravity-wave drag parametrization for numerical climate and weather prediction models. *Atmos. Ocean.* **2003**, *41*, 65–98. [[CrossRef](#)]
9. Alexander, S.P.; Shepherd, M.G. Planetary wave activity in the polar lower stratosphere. *Atmos. Chem. Phys.* **2010**, *10*, 707–718. [[CrossRef](#)]
10. Watanabe, S.; Kawatani, Y.; Tomikawa, Y.; Miyazaki, K.; Takahashi, M.; Sato, K. General aspects of a T213L256 middle atmosphere general circulation model. *J. Geophys. Res. Atmos.* **2008**, *113*, D12110. [[CrossRef](#)]
11. Liu, H.L.; McInerney, J.M.; Santos, S.; Lauritzen, P.H.; Taylor, M.A.; Pedatella, N.M. Gravity waves simulated by high-resolution Whole Atmosphere Community Climate Model. *Geophys. Res. Lett.* **2014**, *41*, 9106–9112. [[CrossRef](#)]
12. Holt, L.A.; Alexander, M.J.; Coy, L.; Molod, A.; Putman, W.; Pawson, S. Tropical waves and the quasi-biennial oscillation in a 7-km global climate simulation. *J. Atmos. Sci.* **2016**, *73*, 3771–3783. [[CrossRef](#)]
13. Liu, X.; Yue, J.; Xu, J.; Garcia, R.R.; Russell, J.M., III; Mlynczak, M.; Wu, D.L.; Nakamura, T. Variations of global gravity waves derived from 14 years of SABER temperature observations. *J. Geophys. Res. Atmos.* **2017**, *122*, 6231–6249. [[CrossRef](#)]
14. Scherllin-Pirscher, B.; Steiner, A.K.; Kirchengast, G.; Kuo, Y.H.; Foelsche, U. Empirical analysis and modeling of errors of atmospheric profiles from GPS radio occultation. *Atmos. Meas. Tech.* **2011**, *4*, 1875–1890. [[CrossRef](#)]
15. Khaykin, S.M.; Hauchecorne, A.; Mzé, N.; Keckhut, P. Seasonal variation of gravity wave activity at midlatitudes from 7 years of COSMIC GPS and Rayleigh lidar temperature observations. *Geophys. Res. Lett.* **2015**, *42*, 1251–1258. [[CrossRef](#)]
16. Leroy, S.S.; Gleisner, H. The stratospheric diurnal cycle in COSMIC GPS radio occultation data: Scientific applications. *Earth Space Sci.* **2022**, *9*, e2021EA002011. [[CrossRef](#)]
17. Kursinski, E.R.; Hajj, G.A.; Schofield, J.T.; Linfield, R.P.; Hardy, K.R. Observing Earth's atmosphere with radio occultation measurements using the Global Positioning System. *J. Geophys. Res. Atmos.* **1997**, *102*, 23429–23465. [[CrossRef](#)]
18. Tsuda, T.; Nishida, M.; Rocken, C.; Ware, R.H. A global morphology of gravity wave activity in the stratosphere revealed by the GPS occultation data (GPS/MET). *J. Geophys. Res.* **2000**, *105*, 7257–7273. [[CrossRef](#)]
19. Ratnam, M.V.; Tetzlaff, G.; Jacobi, C. Global and seasonal variations of stratospheric gravity wave activity deduced from the CHAMP/GPS satellite. *J. Atmos. Sci.* **2004**, *61*, 1610–1620. [[CrossRef](#)]
20. Anthes, R.; Schreiner, W. Six new satellites watch the atmosphere over Earth's equator. *Eos Trans. Am. Geophys. Union* **2019**, *100*. [[CrossRef](#)]
21. Schreiner, W.S.; Weiss, J.P.; Anthes, R.A.; Braun, J.; Chu, V.; Fong, J.; Hunt, D.; Kuo, Y.H.; Meehan, T.; Serafino, W.; et al. COSMIC-2 radio occultation constellation: First results. *Geophys. Res. Lett.* **2020**, *47*, e2019GL086841. [[CrossRef](#)]
22. Pedatella, N.M.; Zakharenkova, I.; Braun, J.J.; Cherniak, I.; Hunt, D.; Schreiner, W.S.; Straus, P.R.; Valant-Weiss, B.L.; Vanhove, T.; Weiss, J.; et al. Processing and validation of FORMOSAT-7/COSMIC-2 GPS total electron content observations. *Radio. Sci.* **2021**, *56*, e2021RS007267. [[CrossRef](#)]
23. Tien, J.Y.; Okiihiro, B.B.; Esterhuizen, S.X.; Franklin, G.W.; Meehan, T.K.; Munson, T.N.; Robison, D.E.; Turbiner, D.; Young, L.E. Next generation scalable spaceborne GNSS science receiver. In Proceedings of the 2012 International Technical Meeting of the Institute of Navigation, Newport Beach, CA, USA, 30 January–1 February 2012; pp. 882–914.
24. Alexander, S.P.; Tsuda, T.; Kawatani, Y.; Takahashi, M. Global distribution of atmospheric waves in the equatorial upper troposphere and lower stratosphere: COSMIC observations of wave mean flow interactions. *J. Geophys. Res.* **2008**, *113*, D24115. [[CrossRef](#)]
25. Anthes, R.A. Exploring Earth's atmosphere with radio occultation: Contributions to weather, climate and space weather. *Atmos. Meas. Tech. Discuss.* **2011**, *4*, 1077–1103. [[CrossRef](#)]
26. Rakshit, G.; Jana, S.; Maitra, A. Gravity wave behavior in lower stratosphere during tropical cyclones over the Bay of Bengal. *Radio. Sci.* **2018**, *53*, 1356–1367. [[CrossRef](#)]
27. Randel, W.J.; Wu, F.; Podglajen, A. Equatorial waves, diurnal tides and small-scale thermal variability in the tropical lower stratosphere from COSMIC-2 radio occultation. *J. Geophys. Res. Atmos.* **2021**, *126*, e2020JD033969. [[CrossRef](#)]

28. Uccellini, L.W.; Koch, S.E. The synoptic setting and possible energy sources for mesoscale wave disturbances. *Mon. Weather Rev.* **1987**, *115*, 721–729. [[CrossRef](#)]
29. Ern, M.; Arras, C.; Faber, A.; Frhlich, K.; Jacobi, C.; Kalisch, S.; Krebsbach, M.; Preusse, P.; Schmidt, T.; Wickert, J. Observations and ray tracing of gravity waves: Implications for global modeling. In *Climate and Weather of the Sun-Earth System (CAWSES) Highlights from a Priority Program*; Lubken, F.J., Ed.; Springer: Dordrecht, The Netherlands, 2013; pp. 383–408. [[CrossRef](#)]
30. Ratnam, M.V.; Babu, A.N.; Rao, V.V.M.J.; Rao, S.V.B.; Rao, D.N. MST radar and radiosonde observations of inertia-gravity wave climatology over tropical stations: Source mechanisms. *J. Geophys. Res. Atmos.* **2008**, *113*, D07109. [[CrossRef](#)]
31. Zhang, Y.; Xiong, J.; Liu, L.; Wan, W. A global morphology of gravity wave activity in the stratosphere revealed by the 8-year SABER/TIMED data. *J. Geophys. Res.* **2012**, *117*, D21101. [[CrossRef](#)]
32. Karoly, D.J.; Roff, G.L.; Reeder, M.J. Gravity wave activity associated with tropical convection detected in TOGA COARE sounding data. *Geophys. Res. Lett.* **1996**, *23*, 261–264. [[CrossRef](#)]
33. Wright, C.J.; Gille, J.C. HIRDLS observations of gravity wave momentum fluxes over the monsoon regions. *J. Geophys. Res.* **2011**, *116*, D12103. [[CrossRef](#)]
34. Jana, S.; Rakshit, G.; Maitra, A. Gravity wave activities associated with convective phenomena at a tropical location near land-sea boundary. *Radio Sci.* **2020**, *55*, e2019RS006952. [[CrossRef](#)]
35. Sato, K.; Dunkerton, T.J. Estimates of momentum flux associated with equatorial Kelvin and gravity waves. *J. Geophys. Res. Atmos.* **1997**, *102*, 26247–26261. [[CrossRef](#)]
36. Vincent, R.A.; Alexander, M.J. Gravity waves in the tropical lower stratosphere: An observational study of seasonal and interannual variability. *J. Geophys. Res.* **2000**, *105*, 17983–17993. [[CrossRef](#)]
37. Rao, D.N.; Thulasiraman, S.; Rao, S.V.B.; Rao, T.N.; Kishore, P.; Ratnam, M.V.; Reddy, K.K. VHF radar observations of tropical easterly jet stream over Gadanki. *Adv. Space Res.* **2000**, *26*, 943–946. [[CrossRef](#)]
38. Vasantha, B.; Ratnam, M.V.; Mohan, K.; Kamala, S.; Rao, D.N.; Rama, G.V. Characteristics of tropical easterly jet over Gadanki: Comparison with radiosonde and rawinsonde. *Indian J. Radio Space Phys.* **2002**, *31*, 130–139.
39. Nath, D.; Ratnam, M.V.M.; Rao, V.V.M.J.; Murthy, B.V.K.; Rao, S.V.B. Gravity wave characteristics observed over a tropical station using high-resolution GPS radiosonde soundings. *J. Geophys. Res.* **2009**, *114*, D06117. [[CrossRef](#)]
40. Fritts, D.C.; VanZandt, T.E. Spectral estimates of gravity wave energy and momentum fluxes. Part I: Energy dissipation, acceleration, and constraints. *J. Atmos. Sci.* **1993**, *50*, 3685–3694. [[CrossRef](#)]
41. Wang, L.; Alexander, M.J. Gravity wave activity during stratospheric sudden warmings in the 2007–2008 Northern Hemisphere winter. *J. Geophys. Res.* **2009**, *114*, D18108. [[CrossRef](#)]
42. Wang, L.; Alexander, M.J. Global estimates of gravity wave parameters from GPS radio occultation temperature data. *J. Geophys. Res. Atmos.* **2010**, *115*, D21122. [[CrossRef](#)]
43. Xu, X.H.; Yu, D.C.; Luo, J. The spatial and temporal variability of global stratospheric gravity waves and their activity during sudden stratospheric warming revealed by COSMIC measurements. *Adv. Atmos. Sci.* **2018**, *35*, 1533–1546. [[CrossRef](#)]
44. Luo, J.; Hou, J.L.; Xu, X.H. Variations of Stratospheric Gravity Waves Derived from Temperature Observations of Multi-GNSS Radio Occultation Missions. *Remote Sens.* **2021**, *13*, 4835. [[CrossRef](#)]
45. Houchi, K.; Stoffelen, A.; Marseille, G.J.; De Kloe, J. Comparison of wind and wind shear climatologies derived from high-resolution radiosondes and the ECMWF model. *J. Geophys. Res.* **2010**, *115*, D22123. [[CrossRef](#)]
46. Budescu, D.V. Dominance analysis: A new approach to the problem of relative importance of predictors in multiple regression. *Psychol. Bull.* **1993**, *114*, 542–551. [[CrossRef](#)]
47. Azen, R.; Budescu, D.V. Comparing predictors in multivariate regression models: An extension of dominance analysis. *J. Educ. Behav. Stat.* **2006**, *31*, 157–180. [[CrossRef](#)]
48. Tonidandel, S.; Lebreton, J.M. Relative Importance Analysis: A Useful Supplement to Regression Analysis. *J. Bus. Psychol.* **2011**, *26*, 1–9. [[CrossRef](#)]
49. Kraha, A.; Turner, H.; Nimon, K.; Zientek, L.R.; Henson, R.K. Tools to support interpreting multiple regression in the face of multicollinearity. *Front. Psychol.* **2012**, *3*, 44. [[CrossRef](#)]
50. Zhang, K.; Sebo, S.; McDonald, W.; Bhaskar, A.; Shuster, W.; Stewart, R.D.; Parolari, A.J. The role of inflow and infiltration (I/I) in urban water balances and streamflow regimes: A hydrograph analysis along the sewershed-watershed continuum. *Water. Resour. Res.* **2023**, *59*, e2022WR032529. [[CrossRef](#)]
51. LeBreton, J.M.; Hargis, M.B.; Griepentrog, B.; Oswald, F.L.; Ployhart, R.E. A multidimensional approach for evaluating variables in organizational research and practice. *Pers. Psychol.* **2007**, *60*, 475–498. [[CrossRef](#)]
52. Sasi, M.N.; Ramkumar, G.; Deepa, V.; Murthy, B.V.K. Inertia-gravity waves associated with tropical easterly jet over the Indian subcontinent during the south west monsoon period. *Geophys. Res. Lett.* **2000**, *27*, 3201–3204. [[CrossRef](#)]
53. Kumar, K.K. VHF radar observations of convectively generated gravity waves: Some new insights. *Geophys. Res. Lett.* **2006**, *33*, L01815. [[CrossRef](#)]
54. Fang, X.; Forbes, J.M.; Benna, M.; Montabone, L.; Curry, S.; Jakosky, B. The origins of longterm variability in Martian upper atmospheric densities. *J. Geophys. Res. Space Phys.* **2022**, *127*, e2021JA030145. [[CrossRef](#)]
55. Romatschke, U.; Medina, S.; Houze, R.A. Regional, seasonal, and diurnal variations of extreme convection in the South Asian region. *J. Clim.* **2010**, *23*, 419–439. [[CrossRef](#)]

56. Qie, X.S.; Wu, X.K.; Yuan, T.; Bian, J.C.; Lu, D.R. Comprehensive pattern of deep convective systems over the Tibetan Plateau–South Asian monsoon region based on TRMM data. *J. Clim.* **2014**, *27*, 6612–6626. [[CrossRef](#)]
57. Zhang, F.; Tao, D. Effects of vertical wind shear on the predictability of tropical cyclones. *J. Atmos. Sci.* **2013**, *70*, 975–983. [[CrossRef](#)]
58. Tsuda, T. Characteristics of atmospheric gravity waves observed using the MU (Middle and Upper atmosphere) radar and GPS (Global Positioning System) radio occultation. *Proc. Jpn. Acad. Ser. B* **2014**, *90*, 12–27. [[CrossRef](#)] [[PubMed](#)]
59. Tao, D.; Zhang, F. Effects of vertical wind shear on the predictability of tropical cyclones: Practical versus intrinsic limit. *J. Adv. Model. Earth Syst.* **2015**, *7*, 1534–1553. [[CrossRef](#)]
60. Miyahara, S.; Hayashi, Y.; Mahlman, J.D. Interactions between gravity waves and planetary-scale flow simulated by the GFDL ‘SKYHI’ general circulation model. *J. Atmos. Sci.* **1986**, *43*, 1844–1861. [[CrossRef](#)]
61. Alexander, S.P.; Tsuda, T.; Kawatani, Y. COSMIC GPS observations of Northern Hemisphere winter stratospheric gravity waves and comparisons with an atmospheric general circulation model. *Geophys. Res. Lett.* **2008**, *35*, 156–167. [[CrossRef](#)]
62. Baldwin, M.P.; Gray, L.J.; Dunkerton, T.J.; Hamilton, K.; Haynes, P.H.; Randel, W.J.; Holton, J.R.; Alexander, M.J.; Hirota, I.; Horinouchi, T.; et al. The quasi-biennial oscillation. *Rev. Geophys.* **2001**, *39*, 179–229. [[CrossRef](#)]
63. Faber, A.; Llamedo, P.; Schmidt, T.; de la Torre, A.; Wickert, J. On the determination of gravity wave momentum flux from GPS radio occultation data. *Atmos. Meas. Tech.* **2013**, *6*, 3169–3180. [[CrossRef](#)]
64. Schmidt, T.; Alexander, P.; de la Torre, A. Stratospheric gravity wave momentum flux from radio occultations. *J. Geophys. Res. Atmos.* **2016**, *121*, 4443–4467. [[CrossRef](#)]

Disclaimer/Publisher’s Note: The statements, opinions and data contained in all publications are solely those of the individual author(s) and contributor(s) and not of MDPI and/or the editor(s). MDPI and/or the editor(s) disclaim responsibility for any injury to people or property resulting from any ideas, methods, instructions or products referred to in the content.